

● *Original Contribution*

## PRODUCING DIFFUSE ULTRASOUND REFLECTIONS FROM MEDICAL INSTRUMENTS USING A QUADRATIC RESIDUE DIFFUSER

JINLAN HUANG,\* PIERRE E. DUPONT,† ADITYA UNDURTI,† JOHN K. TRIEDMAN,\* and ROBIN O. CLEVELAND†

\*Dept. Cardiology, Div. Basic Cardiovascular Research, Children's Hospital Boston, Boston, MA, USA; and

†Aerospace and Mechanical Engineering, Boston University, Boston, MA, USA

(Received 22 July 2005, revised 31 October 2005, in final form 11 November 2005)

**Abstract**—Simultaneous visualization of tissue and surgical instruments is necessary during ultrasound-guided medical procedures. Standard minimally invasive instruments are typically metallic and act as strong specular scatterers. As a result, such instruments saturate the image or disappear according to the angle of incidence, obscuring nearby tissue and making it difficult to determine the instrument's precise location. The objective of this study was to produce diffusive reflections from the surface of surgical instruments for improved visualization in ultrasound. A surface profile based on a 2D quadratic residue diffuser (QRD) was employed, which has been demonstrated to reduce specular reflection in other acoustic applications. The backscattered echo amplitude from the diffusive surface at various angles of insonation was measured and compared to that from unmodified metal surfaces and heart tissue surfaces. The QRD resulted in an 8 dB reduction of the specular signal. Furthermore, the dynamic range for angles up to 75 degrees was less than 20 dB for the QRD and more than 65 dB for a flat surface. The QRD surface produces two beneficial results for the simultaneous imaging of instruments and tissue. First, the conspicuity of diffusive surfaces in ultrasound images is markedly improved in comparison with unmodified metal surfaces. Secondly, the echo amplitude of diffusive metal surfaces differs in mean and standard deviation from that of tissue facilitating image enhancement and segmentation. (E-mail: [jinlan@enders.tch.harvard.edu](mailto:jinlan@enders.tch.harvard.edu)) © 2006 World Federation for Ultrasound in Medicine & Biology.

**Key Words:** Ultrasound-guided interventional procedures, Instrument visibility, Specular reflection, Diffuse reflection, Angle of incidence.

### INTRODUCTION

Ultrasound imaging enjoys widespread use in diagnostic procedures and its use for the guidance of interventional procedures has been growing in popularity owing to its unique real-time capability and submillimeter spatial resolution (Matalon and Silver 1990; Holm and Skjoldbye 1996). The recent introduction of commercial real-time 3D imaging systems is likely to facilitate ultrasound guidance of more complex interventional procedures.

A current impediment to its use, however, is the difficulty encountered in visualizing and navigating metal instruments from ultrasound images. Ultrasound imaging systems are designed to detect the weak acoustic echoes produced by scatterers whose impedance variations are on the order of 10% of the impedance of water.

Simultaneous imaging of metallic instruments (e.g., stainless steel) is a significant challenge because metals have an acoustic impedance approximately ten times that of water. This problem is compounded by the specular nature of reflections arising from the instruments' typically smooth surfaces. The result is that, when imaging an instrument, the ultrasound system receives a very strong echo at normal incidence, which can saturate the image, and almost no signal at oblique incidence, in which case the surface becomes invisible.

The large reflections at the interface mean that tissue behind the tool lies in a shadow region and is not detectable. Reverberation within the instrument can result in multiple echoes from the instrument appearing in the shadow region. In complex scenes, these echoes can be mistakenly interpreted as tissue structures. The strong scattering strength of the instruments also can produce side-lobe artifacts whose strength overwhelms the primary lobe echo from the tissue. Lastly, diffraction from sharp edges of the instrument can result in strong echo

Address correspondence to: Jinlan Huang, Children's Hospital Boston, Dept. Cardiology, Div. Basic Cardiovascular Research, Enders 13, 320 Longwood Avenue, Boston, MA 02115, USA. E-mail: [jinlan@enders.tch.harvard.edu](mailto:jinlan@enders.tch.harvard.edu)

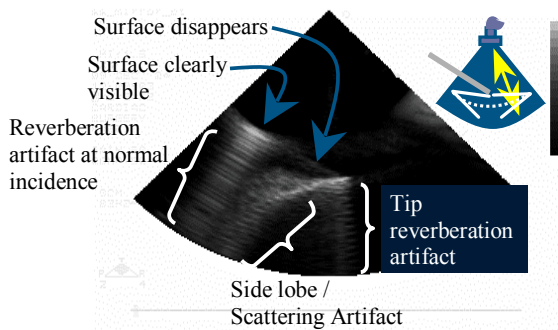


Fig. 1. Visualization problems for a 4 mm diameter stainless steel rod in water. The rod's axis is 30 degrees from horizontal as shown in the schematic in the upper right.

signals that obscure the location of the scattering edge. Several of these effects are demonstrated in Fig. 1. They make it difficult to determine an instrument's location, orientation and geometry while simultaneously imaging tissue.

Of the two problems impacting instrument imaging, namely impedance mismatch and specularity, this paper addresses the latter. Reduction in specularity, by redistributing echo energy over all reflection angles, directly addresses the problem of instrument disappearance at oblique angles, and can also reduce reverberation.

In the literature, attention has principally been focused on enhanced visualization of needles by creating a global increase in echogenicity. Most commonly, addition of inhomogeneity to an otherwise smooth instrument to improve visualization of the entire needle shaft at different insonation angles is proposed. Various modifications involve roughening or scoring of a portion of the needle (Hopkins and Bradley 2001; Nichols et al. 2003) or insertion of a screw stylet (Reading et al. 1987; Reading et al. 1988). Roughening the outer surface is as good as (Heckemann and Seidel 1983) or better than (McGahan 1986) roughening the inner stylet for enhancing visualization.

It also has been reported that large structure changes (e.g., aspiration ports or introduction of air bubbles) may enhance tip echo (Hurwitz and Nageotte 1989; Bondestam 1992; Schwarzacher et al. 1998). Application of a layer of polymeric coating that entraps bubbles of air in microcavities also provides increased acoustical scattering. When applied to the entire length of the needle shaft, this approach can provide a significantly brighter ultrasound image of the device at virtually any angle with respect to the transducer (Gottlieb et al. 1998; Culp et al. 2000; Hopkins and Bradley 2001; Nichols et al. 2003).

Signal and image processing techniques have also been proposed to increase needle-tip visibility. These include placing a sensor at the needle tip to determine tip location (Winsberg et al. 1991; Perrella et al. 1992) or

employing the electronic beam steering available in most diagnostic scanners to angle the beam so that it is always steered perpendicular to the needle (Baker 1999; Cheung and Rohling 2004). The brightened needle in the steered image is then fused with the original image to produce an improved image. Some other sonographic modalities have also been explored including the use of compound imaging (Cohen et al. 2003) and color Doppler to detect motion of an actively vibrated needle (Kurohiji et al. 1990; Hamper et al. 1991; Longo et al. 1992; Gerscovich 1994; Cockburn and Cosgrove 1995; Feld et al. 1997; Jones et al. 1997).

Most of these prior studies were limited to needles, and their analyses were primarily based on image quality. Without quantification of surface features and evaluation of the underlying acoustic phenomena, it is difficult to compare techniques covered in different papers or to ascertain the fundamental improvement limits such approaches may provide. The approach taken in this paper is to construct a theoretically ideal, quantitatively defined diffuse instrument surface and to experimentally characterize its performance both quantitatively in terms of diffusive scattering and qualitatively in terms of image quality.

#### Diffusive scattering

The ideal diffuse reflector will scatter an incoming wave equally in all directions, as illustrated in Fig. 2. For a focused ultrasound source, the incident signal can be modeled, to first order, as a progressive wave with uniform amplitude over a cone of angle  $\alpha = 2\arcsin(d/2r)$  in which  $d$  is the aperture diameter and  $r$  is the focal length in which case the incident energy is proportional to  $p_I^2\Omega$  where  $\Omega = 2\pi[1 - \cos(\alpha/2)]$  is the solid angle of the cone of the incident beam and  $p_I$  is the pressure amplitude of the incident beam. An ideal diffusive surface will scatter the acoustic energy uniformly over a solid angle of  $2\pi$ , that is, the reflected energy will be proportional to  $p_R^2 2\pi$  where  $p_R$

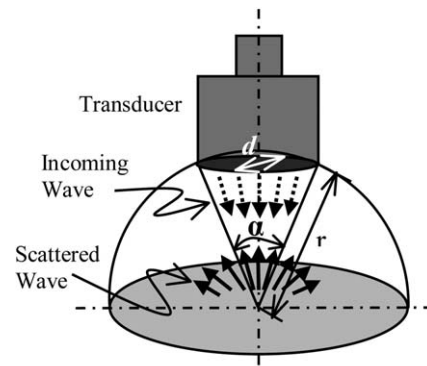


Fig. 2. Ideal diffusive scattering.

is the pressure amplitude of the reflected wave. If the surface is rigid, that is, one that does not allow acoustic energy to be transmitted into it, then the incident and scattered energies must be equal and hence the amplitude of the reflected is  $p_R = \sqrt{1-\cos(\alpha/2)} \cdot p_I$ .

For example, the transducer employed in this study had an aperture diameter  $d = 25.4$  mm and focal length  $r = 78$  mm, which results in  $\alpha = 18.7^\circ$  and the solid angle of the incident beam is 1.33% of  $2\pi$ . Therefore, an ideally diffusive surface would result in the pressure signal received by the transducer that is 11.5% of the incident signal or  $-18.7$  dB.

The diffuse reflector problem has been addressed in architectural acoustics to reduce the “acoustic glare” associated with large flat walls. While simply roughening surfaces increases their diffusivity, the quadratic residue diffuser (QRD), which analytically predicts uniform scattering of an incident plane wave (Schroeder 1979; D’Antonio and Cox 2000), has proven effective in practice. In this approach, the wall surface is composed of wells of constant width and varying depth. Well width  $w$  is selected as a small fraction of incident wavelength  $\lambda$  (typically one-tenth of a wavelength). To obtain uniform scattering, well depth is chosen proportional to a quadratic residue sequence,  $S_n = n^2 \bmod N$ , where  $N$  is a selected odd prime number and the index  $n = 1, \dots, K$ , where  $K$  is the number of wells. For a one-dimensional QRD, the well depth,  $d(x_n)$ , at position  $x_n$ , is given by

$$d(x_n) = \frac{\lambda}{2} \times \frac{S_n}{N} \quad (1)$$

The sequence and, consequently, the well depths have periodicity  $N$ . While the effective bandwidth of the QRD increases with  $N$  (Schroeder 1979), the assumption of incident wave planarity limits  $N$  to values such that the wave is approximately planar over the sequence well width,  $Nw$ .

A 2D QRD can be constructed by superposition of two one-dimensional QRD’s in each coordinate direction,

$$d(x_n, y_m) = \frac{\lambda}{2} \times \left( \frac{S_n}{N} + \frac{S_m}{M} \right) \quad (2)$$

While the two sequences can be different, they are typically the same, *i.e.*,  $N = M$ .

## MATERIALS AND METHODS

A two-dimensional QRD was designed for a 3.5 MHz central frequency transducer. The corresponding wavelength in water is approximately  $\lambda = 430$   $\mu\text{m}$ . QRD theory assumes that well width satisfies  $w \ll \lambda$ , that the wells are typically square and that there is no separation

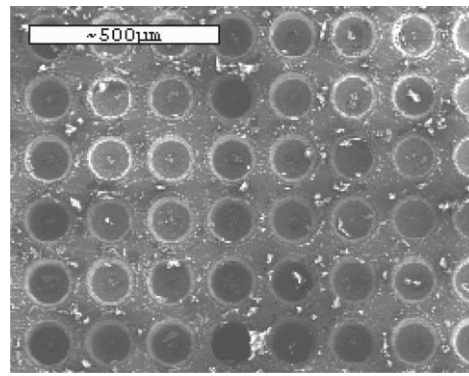


Fig. 3. SEM photograph of a 2D QRD as manufactured.

between adjacent wells. Manufacturing constraints, however, led to the use of a 100  $\mu\text{m}$  diameter drill bit to machine the wells. This resulted in wells of circular cross section and width  $w = 100 \mu\text{m} = 0.23\lambda$ . Furthermore, to avoid bit breakage, the well center-to-center distance was 150  $\mu\text{m}$  leading to a separation distance between wells of 50  $\mu\text{m}$  in the two coordinate directions and 112  $\mu\text{m}$  on the diagonal.

Two periods of an  $N = 17$  sequence (that is,  $K = 34$ ) were constructed on an aluminum block (58  $\times$  13  $\times$  22 mm), a portion of which is shown in Fig. 3. The length of one QRD sequence is  $17 \times 150 \mu\text{m} = 2.5$  mm, which falls within the 1 to 3 mm range of the typical image plane focal beam width. The well depths vary from 0 to 415  $\mu\text{m}$ .

As a baseline for comparison, a second surface was manufactured with the same well width and spacing, but with a uniform well depth of 100  $\mu\text{m}$ , or approximately one quarter wavelength. In this design, the unmachined areas located diagonally between wells can be viewed as wells of zero depth. This design can be anticipated to reduce the surface reflection coefficient  $R$  through half wavelength interference. This design is referred to as the uniform depth array (UDA).

The performance of the QRD and UDA surfaces was compared with cardiac tissue. Image-guided beating-heart repair of congenital cardiac defects represent an important class of interventions which can benefit from improved instrument visualization (Suematsu *et al.* 2004). Fresh porcine heart tissue was obtained from male Yorkshire pigs (70 to 80 kg, 5- to 6-mo old). These tests were performed as secondary use of the tissue and the animals were treated using a protocol approved by the Animal Care and Use Committee of Children’s Hospital, Boston. The porcine heart was immediately placed in a container of 1% phosphate buffered saline (PBS) solution at 37°C. A sample of the heart wall was then cut from the heart and sutured onto a ring (35 mm in diameter for left atrium, 70 mm in diameter for left and right

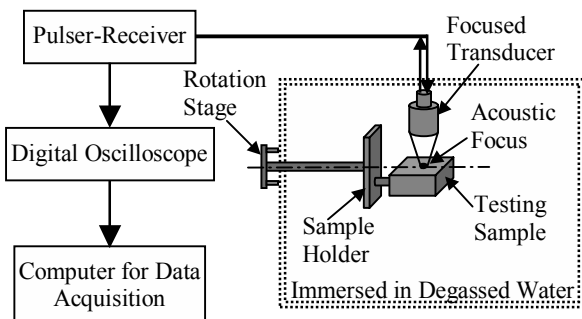


Fig. 4. Schematic of measurement apparatus.

ventricles). By this method, a relatively flat and smooth surface of tissue sample could be obtained. The ring and sample were then immediately transferred to the ultrasound tank (prefilled with 1% PBS solution heated to 37°C). All measurements were carried out within 2 h. Echo measurements are reported for the exterior free wall of the left atrium, the left ventricle and the right ventricle.

A schematic of the apparatus for the ultrasound measurements is shown in Fig. 4. The acoustic source and test sample were immersed in water contained in an acrylic tank (50 × 30 × 30 cm) which was open to the atmosphere. The bottom of the tank was lined with a layer of silicone rubber to reduce acoustic reflections. For measurements on metal surfaces the tank was filled with filtered, deionized, degassed water and for measurements on tissue the tank was filled with PBS as described above.

The acoustic source was a single-element, spherically focused piezoceramic transducer (Model V380-SU, Panametrics-NDT, Waltham, MA) with a focal length of 78 mm, an aperture of 25.4 mm and a center frequency of 3.5 MHz. The transducer was driven by a pulser-receiver (Model 5077PR-15-U, Panametrics-NDT, Waltham, MA) with the following settings: pulser voltage 100 V, transducer frequency 3.5 MHz. The pulser was used in pulse-echo mode and the received backscattered signals were amplified by the receiver circuitry. The signal was recorded by a digital oscilloscope (Model TDS 1002, Tektronix, Portland, OR) with 60 MHz bandwidth and the maximum 1GS/s sampling frequency. Waveforms from the oscilloscope were transferred to a computer for off-line processing. The backscattered data were processed in a similar manner to that carried out in diagnostic scanners. The envelope of the A-line was obtained from the magnitude of the Hilbert transform of the signal. Time gating was employed to select the reflections from the region of interest (ROI).

A 3D positioning system mounted on the top of the tank was used to move the transducer to the desired

location. A rotation stage was mounted on the side of the tank with a mounting post fixed to the center of the stage. The post went through the tank wall (an O-ring was used to avoid leakage) and the sample was mounted to the post using appropriately designed holders. The sample was positioned so that the surface to be interrogated was along the axis of the rotational stage. Rotation of the sample allowed the angle on insonation to be varied without affecting the distance between the sample and the transducer. Unless otherwise noted, the angle of insonation was varied from  $-75^\circ$  to  $75^\circ$  at  $5^\circ$  increments with the increments reduced to  $1^\circ$  for  $-15^\circ$  to  $15^\circ$ .

## RESULTS

Figure 5 plots the maximum echo amplitude as a function of incident angle for a plane surface, QRD and UDA. The results were normalized by the echo amplitude of a reference waveform measured from a rigid plane surface at normal incidence. Each data point is the average of measurements at five different locations, and the error bars indicate the standard deviation. Also depicted is the angle-independent echo amplitude for a rigid ideal diffuse surface ( $-18.7$  dB for this transducer).

For the planar surface, the backscattered signal was maximal for normal incidence and reduced to approximately  $-65$  dB for angles of incidence greater than 20 degrees. This substantial decrease in signal strength is consistent with reflection from a specular surface given that the electronic noise floor was  $-65$  dB. In contrast, the maximum QRD amplitude (at normal incidence) was  $-8$  dB and fell by only 20 dB to  $-28$  dB as the angle of incidence increased to  $75^\circ$ . While substantially more diffusive than the planar surface, performance of the QRD does deviate from the constant  $-18.7$  dB of an ideal diffuser, owing to the practical limitations involved

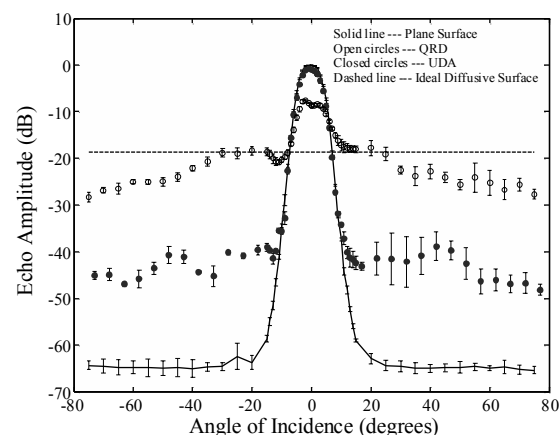


Fig. 5. Echo amplitude versus angle of incidence of planar metal surface, QRD, UDA and ideal diffuse reflector.

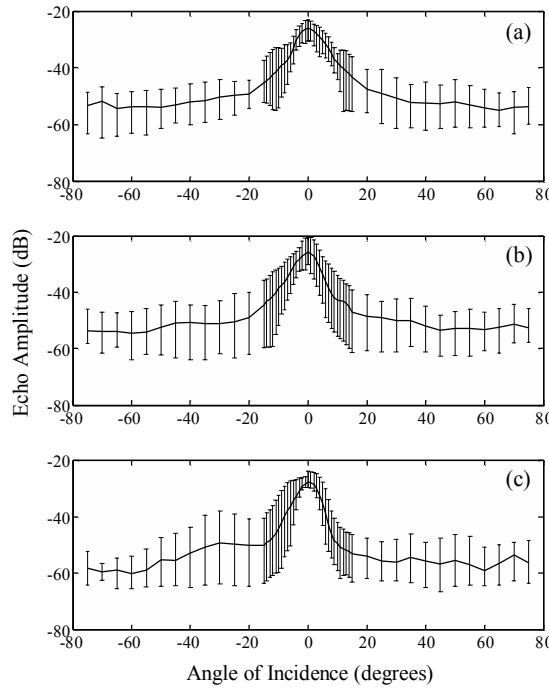


Fig. 6. Echo amplitude versus angle of incidence for cardiac tissue. (a) Left atrium; (b) Left ventricle; (c) right ventricle.

in its manufacture. In particular, the required shape and spacing of the wells means that they only account for 35% of the surface area, leaving 65% planar. The compressed dynamic range of 20 dB for the QRD in comparison to 65 dB for a planar surface, however, represents a substantial improvement.

The results from the UDA show a normal incidence echo amplitude similar to that of the planar surface and for nonnormal incidence, the backscattered signals fall about half-way between that of the QRD and the planar surface. This indicates that the performance of the QRD cannot be attributed simply to the presence of wells, but also depends on the distribution of well depths.

To evaluate the performance of the QRD in a medical imaging context, measurements were made using porcine tissue from the exterior free walls of the left atrium, left ventricle and right ventricle of fresh porcine tissue. The results are shown in Fig. 6 with the echo amplitude referenced to that of the planar metal surface. Each data point is the average of measurements conducted at two different locations of tissue samples from three different pigs, and the error bars indicate the total range of the measurements.

Since the three cardiac tissue types produce similar echo profiles, their mean echo amplitude is plotted for comparison to the QRD and planar metal surface in Fig. 7. The mean tissue response displays a specular reflection characteristic, but with a dynamic range of about 25

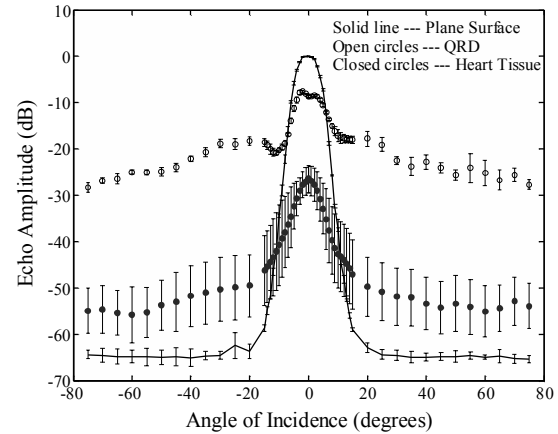


Fig. 7. Echo amplitude versus angle of incidence for the QRD, planar metal surface and mean of the cardiac tissues in Fig. 6.

dB compared to about 65 dB for the planar metal surface. This is to be expected since the inhomogeneities in the tissue provide a background scattering signal that is insensitive to incident angle. This background level raises the tissue echo amplitude for large incident angles at least 10 dB higher than that of the planar metal surface. (Recall that the latter is limited by the noise floor).

The imaging performance of the QRD surface was evaluated using a clinical echo cardiography machine with a 4 MHz probe (Philips SONOS 7500 and  $\times 4$  probe). The probe was used to scan the planar metal surface, the QRD and the exterior free wall of the right ventricle. The echo machine settings were selected to optimize tissue images and subsequently held constant for all surfaces (focal length, 6 cm; depth, 8 cm; gain, 60; compression, 75). Each sample was rotated in the scan plane of the probe as shown in Fig. 8. Images were taken at 5 degree increments over a range of 0 to 60 degrees. Because this is a sector scan probe, only a small region of the sample below the probe is insonified at the desired angle. The angle of incidence was limited to less than 7 degrees by restricting the field of view of the images to a rectangle of size  $15 \times 10$  mm.

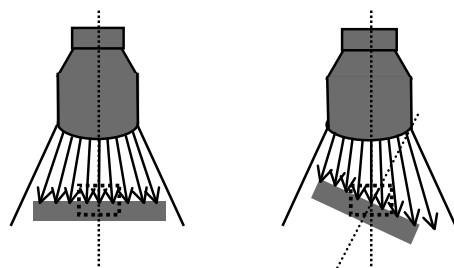


Fig. 8. Schematic of imaging probe and target depicting imaging rectangle.

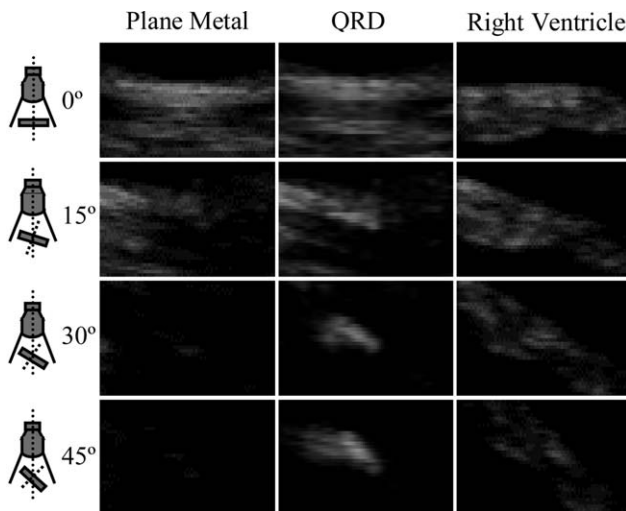


Fig. 9. 2D ultrasound images of a planar metal surface, QRD and porcine right ventricle at various angles of incidence.

The images of planar metal surface, QRD and tissue are shown in Fig. 9 at 15 degree increments. As was expected, based on data from the echo amplitude plots, the planar surface disappears completely for angles greater than approximately 20 degrees. In Fig. 9, the QRD covers about the middle third of the surface with planar surfaces on each side. The QRD remains visible over the entire range of angles even though the planar surface to its left and right disappears. The right ventricle is also visible over the entire range of angles although its surface does start to drop out at larger angles.

To verify that the single-element transducer results of Fig. 7 are comparable to those obtained from an ultrasound imaging system, the mean pixel intensity versus incident angle was computed for the surfaces shown in Fig. 9. For all surfaces, the length of the region of interest used to compute the mean corresponded to the length of the QRD (5 mm). The results, plotted in Fig. 10, confirm the single-element transducer tests, that is, the QRD substantially reduces the dynamic range of metal surface reflections and produces a mean level higher than that of tissue.

As described in the introduction, a variety of effects in addition to specularity impact instrument visualization. These include strong side-lobe echoes, edge scattering artifacts, shadows and reverberation. Of these, the diffusive scattering of the QRD only reduces reverberation. For example, side-lobe artifacts from the QRD can be observed in Fig. 9. They occur because the QRD surface is still a much stronger scatterer than tissue and can, therefore, produce an appreciable echo even when outside the main lobe of the transducer. It is anticipated that edge diffraction artifacts will be similarly unaffected

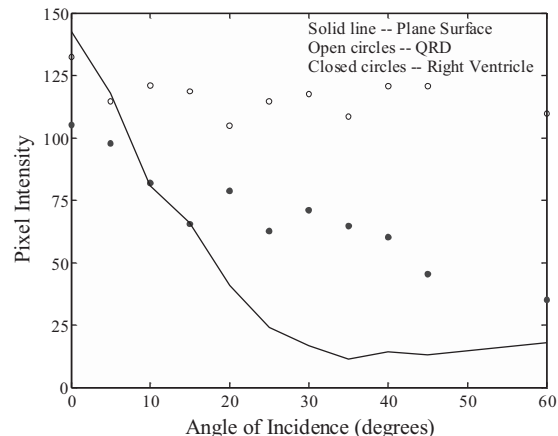


Fig. 10. Mean pixel intensity versus angle of incidence for planar metal surface, QRD and right ventricle.

by a diffusive surface since they are primarily controlled by edge curvature.

Reverberation, however, is markedly reduced by the QRD. Its rough surface distorts the wavefront entering and leaving the instrument and so prevents multiple reflections from producing coherent echoes to the probe. This is demonstrated by the 2D images in Fig. 11 where the reverberation signal below the QRD is weaker than the signal below a plane surface made of the same material and of the same thickness.

## DISCUSSION

This paper provides a quantitative and qualitative evaluation of the effect of specularity on ultrasound imaging of medical instruments. Furthermore, it demonstrates the efficacy of a QRD at ultrasound length scales. Despite size-related fabrication constraints, the QRD manufactured here resulted in backscattered amplitude at oblique angles that was at least 40 dB above that of a planar surface, while the normal incidence amplitude was reduced by 8 dB. This reduction in specularity greatly enhances surface visibility in ultrasound images insonified at oblique angles. While the manufacturing process employed here is impractical for general use, the

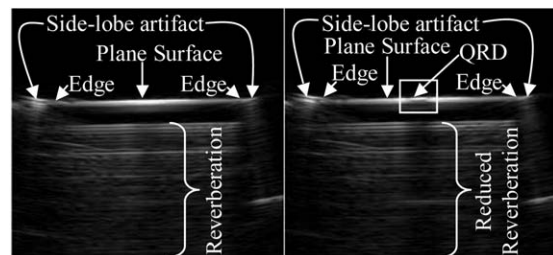


Fig. 11. Effect of QRD on reverberation artifact.

QRD's performance provides a benchmark against which alternate techniques for reducing specular reflections can be compared.

A second advantage of diffusive surfaces is that they turn the impedance mismatch of metal instruments into an advantage for simultaneous imaging with tissue. By greatly compressing the dynamic range of echo amplitude, as illustrated in Fig. 7, diffusivity has separated the echo amplitude mean and standard deviation of the instrument from that of the tissue. This has important implications for enhanced imaging as well as image-based segmentation algorithms. It would permit, for example, imaging schemes in which gain settings are alternated between lower values best suited for instrument imaging and higher values best suited for tissue imaging—without fear of dropout due to echo magnitude overlap. Simple threshold-based image segmentation methods may also be possible.

**Acknowledgements**—This work was supported by NIH NIBIB 1 RO1 EB003052 and NIH Bioengineering Research Partnership grant R01 HL073647. The authors thank Professor Andre Sharon and Mr. Doug Foss of Boston University's Fraunhofer Center for Manufacturing Innovation, along with Theresia Becker for fabricating the test surfaces. Thanks are also due to Drs. Nikolay Vasilyev and Yoshihiro Suematsu for providing tissue samples and to Professor Ronald Roy for his generosity with equipment and technical advice.

## REFERENCES

Baker JA, Soo MS, Mengoni P. Sonographically guided percutaneous interventions of the breast using a steerable ultrasound beam. *Am J Roentgenol* 1999;172(1):157–159.

Bondestam S. The needle tip echo. *J Ultrasound Med* 1992;11(6): 253–256.

Cheung S, Rohling R. Enhancement of needle visibility in ultrasound-guided percutaneous procedures. *Ultrasound Med Biol* 2004;30(5): 617–624.

Cockburn JF, Cosgrove DO. Device to enhance visibility of needle or catheter tip at color Doppler US. *Radiology* 1995;195(2):570–572.

Cohnen M, Saleh A, Luthen R, Bode J, Modder U. Improvement of sonographic needle visibility in cirrhotic livers during transjugular intrahepatic portosystemic stent-shunt procedures with use of real-time compound imaging. *J Vasc Interv Radiol* 2003;14(1):103–106.

Culp WC, McCowan TC, Goertzen TC, et al. Relative ultrasonographic echogenicity of standard, dimpled, and polymeric-coated needles. *J Vasc Interv Radiol* 2000;11(3):351–358.

D'Antonio P, Cox TJ. Diffusor application in rooms. *Appl Acoust* 2000;60:113–142.

Feld R, Needleman L, Goldberg BB. Use of needle-vibrating device and color Doppler imaging for sonographically guided invasive procedures. *Am J Roentgenol* 1997;168(1):255–256.

Gerscovich EO, Budenz RW, Lengle SJ. Assessment of catheter placement and patency by color Doppler ultrasonography. *J Ultrasound Med* 1994;13(5):367–370.

Gottlieb RH, Robinette WB, Rubens DJ, et al. Coating agent permits improved visualization of biopsy needles during sonography. *Am J Roentgenol* 1998;171(5):1301–1302.

Hamper UM, Savader BL, Sheth S. Improved needle-tip visualization by color Doppler sonography. *Am J Roentgenol* 1991;156(2):401–402.

Heckemann R, Seidel KJ. The sonographic appearance and contrast enhancement of puncture needles. *J Clin Ultrasound* 1983;11(5): 265–268.

Holm HH, Skjoldbye B. Interventional ultrasound. *Ultrasound Med Biol* 1996;22(7):773–789.

Hopkins RE, Bradley M. In-vitro visualization of biopsy needles with ultrasound: A comparative study of standard and echogenic needles using an ultrasound phantom. *Clin Radiology* 2001;56(6):499–502.

Hurwitz SR, Nageotte MP. Amniocentesis needle with improved sonographic visibility. *Radiology* 1989;171(2):576–577.

Jones CD, McGahan JP, Clark KJ. Color Doppler ultrasonographic detection of a vibrating needle system. *J Ultrasound Med* 1997; 16(4):269–274.

Kurohiji T, Sigel B, Justin J, Machi J. Motion marking in color Doppler ultrasound needle and catheter visualization. *J Ultrasound Med* 1990;9(4):243–245.

Longo JM, Bilbao JI, Rousseau HP, et al. Color Doppler-US guidance in transjugular placement of intrahepatic portosystemic shunts. *Radiology* 1992;184(1):281–284.

Matalon TA, Silver B. US guidance of interventional procedures. *Radiology* 1990;174(1):43–47.

McGahan JP. Laboratory assessment of ultrasonic needle and catheter visualization. *J Ultrasound Med* 1986;5(7):373–377.

Nichols K, Wright LB, Spencer T, Culp WC. Changes in ultrasonographic echogenicity and visibility of needles with changes in angles of insonation. *J Vasc Interv Radiol* 2003;14(12):1553–1557.

Perrella RR, Kimme-Smith C, Tessler FN, Ragavendra N, Grant EG. A new electronically enhanced biopsy system: value in improving needle-tip visibility during sonographically guided interventional procedures. *Am J Roentgenol* 1992;158(1):195–198.

Reading CC, Charboneau JW, Felmlee JP, James EM. US-guided percutaneous biopsy: use of a screw biopsy stylet to aid needle detection. *Radiology* 1987;163(1):280–281.

Reading CC, Charboneau JW, James EM, Hurt MR. Sonographically guided percutaneous biopsy of small (3 cm or less) masses. *Am J Roentgenol* 1988;151(1):189–192.

Schroeder MR. Binaural dissimilarity and optimum ceilings for concert halls: More lateral sound diffusion. *J Acoust Soc Am* 1979;65(4): 958–963.

Schwarzacher SP, Fitzgerald PJ, Metz JA, et al. Enhancement of spatial orientation of intravascular ultrasound images with side holes in guiding catheters. *Am Heart J* 1998;135(6 Pt 1):1063–1066.

Suematsu Y, Marx G, Stoll J, et al. Three-dimensional echocardiography—guided beating-heart surgery without cardiopulmonary bypass: A feasibility study. *J Thorac Cardiovasc Surg* 2004;128(4): 571–578.

Winsberg F, Mitty HA, Shapiro RS, Yeh HC. Use of an acoustic transponder for US visualization of biopsy needles. *Radiology* 1991;180(3):877–878.